scientific reports

Check for updates

OPEN

Role of ionization potential depression for generation of strongly coupled plasmas in high-pressure supercritical fluids

Juho Lee[1], Hyojeong Lee[2], Suho Kim[2], Hyyong Suk[2] & Gunsu Yun[1,3]✉

The photosphere, one of the Sun's inner layers, and white dwarfs exist as plasmas with high electron density and relatively low temperature, satisfying the strongly coupled condition that the Coulomb coupling parameter exceeds unity. While strongly coupled plasmas are prevalent throughout space, it is difficult to produce and sustain such states in the laboratory with a sufficiently long lifetime for investigation of basic transport processes. To surmount these obstacles, we have developed a laser-produced plasma experiment in supercritical fluids of He, Ar, and Kr. For helium at 100 bar, a nanosecond laser pulse generates a strongly coupled plasma with an electron density, estimated from ionization potential depression (IPD) modeling, of approximately 10^{27} m^{-3}, and a temperature of about 1 eV, corresponding to a Coulomb coupling parameter of 4. Systematic experiments with other species show that the pivotal factor for achieving strongly coupled plasmas is the degree of IPD. This study shows the potential to facilitate precise measurements of thermodynamic transport parameters and equation of state for dense plasma states.

Strongly coupled plasma (SCP) states are prevalent in the universe, as in the core of Jovian planets[1], white dwarfs[2,3], and inner layers of the Sun[4,5]. In SCPs, the average Coulomb potential of charged particles exceeds their average thermal kinetic energy, that is, the Coulomb coupling parameter $\Gamma = (e^2/4\pi\varepsilon_0 k_B T_e)(4\pi n_e/3)^{1/3} \geq 1$, where $e, \varepsilon_0, k_B, T_e$, and n_e are the electron charge, vacuum permittivity, Boltzmann constant, electron temperature, and electron density, respectively[1,6]. On the other hand, more familiar plasmas with relatively low density and high temperature are weakly coupled, i.e., with $\Gamma \ll 1$. SCPs with high density are often created within celestial bodies where strong gravity comes into play. Even in the atmosphere of Jupiter, vigorous lightning generates an SCP state. Although SCPs are ubiquitous across the universe, understanding their characteristics has been a challenging task, since the standard plasma physics theories suitable for the weakly coupled plasmas fail to describe strongly coupled systems.

For decades, theoretical models and numerical simulations have been developed to describe the particle interactions in SCPs, while the basic equation of states (EOS) is yet to be verified by experiments. The experimental approach has been challenging because of the necessity of achieving a high plasma density to satisfy the $\Gamma > 1$ criterion, which demands a considerable amount of energy input. Even if a high-density plasma state is established, measurements of the basic plasma parameters and complex collisional processes among charged particles have remained a significant challenge. Theoretical approaches have adopted collision operators specifically designed for dense plasmas[7,8]. Molecular dynamics simulations have contributed to understanding of transport processes in SCPs, such as diffusion coefficient[9,10] and stopping power[11]. Yet, strongly coupled plasmas are rife with many unsolved and untouched problems.

To achieve a high-density plasma, many experimental approaches adopt solid targets[12] with a high-power laser pulse. However, the solid targets have several limitations including the inevitable occurrence of target damage and short plasma lifetime. Furthermore, when the laser pulse ablates the surface, the vaporized hot particles expand rapidly, making the strongly coupled regime less attainable. To mitigate this issue, we have developed an experimental platform using supercritical fluids as medium for the following reasons. (1) Unlike solid targets, supercritical fluids enhance experimental repeatability by avoiding the risk of target damage. (2) Plasma generation in supercritical fluids would require less power than solid or liquid medium owing to the

[1]Department of Physics, Pohang University of Science and Technology, Pohang, Republic of Korea. [2]Department of Physics and Photon Science, Gwangju Institute of Science and Technology, Gwangju, Republic of Korea. [3]Division of Advanced Nuclear Engineering, Pohang University of Science and Technology, Pohang, Republic of Korea. ✉email: gunsu@postech.ac.kr

absence of a phase transition. Moreover, (3) Supercritical fluids inherently possess higher densities compared to gases, and (4) their lower ionization threshold allows for the efficient utilization of laser energy[13].

The short lifetime of the strongly coupled state in conventional laser plasma experiments is another challenge for reliable observation of particle and energy transport processes and determination of the equation of state. In our previous study[14], an interesting method has been demonstrated to enhance the charge and energy confinement of SCPs using an inhomogeneous pure argon supercritical fluid[15] as a medium. The medium is characterized by a dense population of long-lived submicron-size droplets and nano-size clusters, which can be measured by the medium's opacity in the visible range. It has been reported that droplets and clusters influence charge and energy transport in the plasma and extend its relaxation time up to about a microsecond[14]. This effect is attributed to their role as an energy reservoir, which enhances photon confinement in the optically dense plasma and slows radiative energy loss, thereby prolonging plasma persistence.

However, there was a limitation on the extension of the plasma lifetime because the number of clusters and droplets, which play a key role in prolonging the plasma lifetime, cannot be precisely controlled. They are generated at the end of the compressor through an adiabatic expansion process that introduces significant uncertainty, and their abundance strongly depends on the gas species. For example, krypton forms many clusters, whereas helium generates very few. These factors make it difficult to consistently control or maintain the inhomogeneity and opacity of the supercritical fluid.

In the present work, we introduce an effective generation of SCPs by varying the species composition of supercritical fluids. We examine the relation between the ionization potential depression and the plasma parameters. We show that our experimental approach allows much easier access to high electron density and paves the way toward long-lived SCPs and determination of their EOS.

Results

Experimental apparatus and conditions

The formation of high-pressure supercritical fluids begins at the compressor. The compressor has two pistons with check valves inside. The pistons are connected to a rotating motor, allowing them to undergo repetitive compressing motion. When the pressure reaches 300 bars, the check valve opens, ejecting the compressed gas. This compression-expansion cycle repeats at a rate of 4 Hz. The compressor and the high-pressure chamber are connected by hoses, enabling the pressure of the chamber to reach up to 300 bars from atmospheric pressure. At the outlet of the compressor, the compressed gas undergoes nearly isentropic expansion, resulting in a significant temperature drop. Throughout this process, particles comparable to liquid density are generated extensively. As the pressure inside the chamber gradually increases and reaches the critical pressure, transitioning to the supercritical fluid phase, the droplets and clusters can survive for an extended period - over an hour[15,16]. The presence of these particles is known to significantly influence the energy transport characteristics within the plasma[14]. After pressurization, the droplets and clusters gradually evaporate into the background and mostly disappear an hour later. In this work, plasmas are generated at least an hour after pressurization to exclude the effect of these particles, which vary with the gas species and strongly influence the opacity. This allows us to focus on the intrinsic plasma behavior determined by the atomic species. The phase diagram for noble gases - helium, argon, and krypton - can be found in Fig. 1a. At room temperature and 100 bars of pressure, these fluids exhibit differences in density (Fig. 1b).

Plasmas are generated using an Nd:YAG pulse laser ($\lambda = 1064\,\mathrm{nm}$, $t = 6$ ns, $f = 2$ Hz, and $\varepsilon = 650$ mJ/pulse). The laser pulse is focused at the center of the high-pressure chamber by a convex lens with a focal length of 50 mm. At the focal point, the intensity reaches about 2.5 $\mathrm{TW/cm^2}$ (with a beam waist of about 37 μm). Due to the high-intensity laser, a rapid increase in free electrons occurs during the initial stages of plasma generation. As a result, a significant portion of the laser pulse is consumed in plasma formation, while some is reflected. Slight variations in the extent of energy coupling are observed depending on the noble gas species. Considering the approximately 5.5% reflection from each surface of the sapphire windows, laser energies of 430 mJ, 450 mJ, and 468 mJ are coupled to generate plasma within helium, argon, and krypton supercritical fluid, respectively (with scattering from the different species being negligible). The shot-to-shot fluctuation of the laser pulse is negligible, and the fluctuation in the coupled energy to the medium is less than 3%. Since the laser-produced plasma is short-lived, an ICCD camera with a minimum gate width of 3 ns is used to capture the rapid relaxation process of the plasma. The high-pressure chamber is equipped with sapphire windows that transmit light above the wavelength of 200 nm, enabling various optical diagnostics, such as imaging and optical emission spectroscopy (OES). For OES, plasma emission is collected by a lens and directed to a monochromator (focal length: 300 mm, grating: 300 gr/mm) via an optical fiber. The collection area is 0.46 $\mathrm{mm^2}$. A comprehensive description of the entire apparatus and further details of the acquisition setup are provided in the supplementary materials.

Formation of laser-produced plasmas in supercritical fluids

In the case of laser-produced plasma generated by the nanosecond pulse laser, a jet-like shape is observed. Figure 2 shows the plasma generation and relaxation in various supercritical fluids. The time-resolved images reveal that the plasma ignites at the laser focal point, with backward expansion occurring from -10 ns to 0 ns, where the time zero is defined at the moment of the maximum plasma emission intensity. This expansion occurs in a kind of ionization wave, facilitated by pre-ionization within the converging laser envelope, in which seed electrons are produced by ionization of atoms by the laser pulse and excited atomic species are also generated. Since the plasma frequency at the focal point exceeds the optical frequency of the laser, the expansion is constrained to the backward direction. The emission intensity from the plasma reaches a peak when the expansion ceases. The time-resolved ICCD camera images show that the plasma emission persists for an extended period of time, long after the 6 ns laser pulse having passed the plasma ignition point at -10 ns. While the helium plasma dissipates in approximately 10 ns, the argon and krypton plasmas persist much longer than 10 ns.

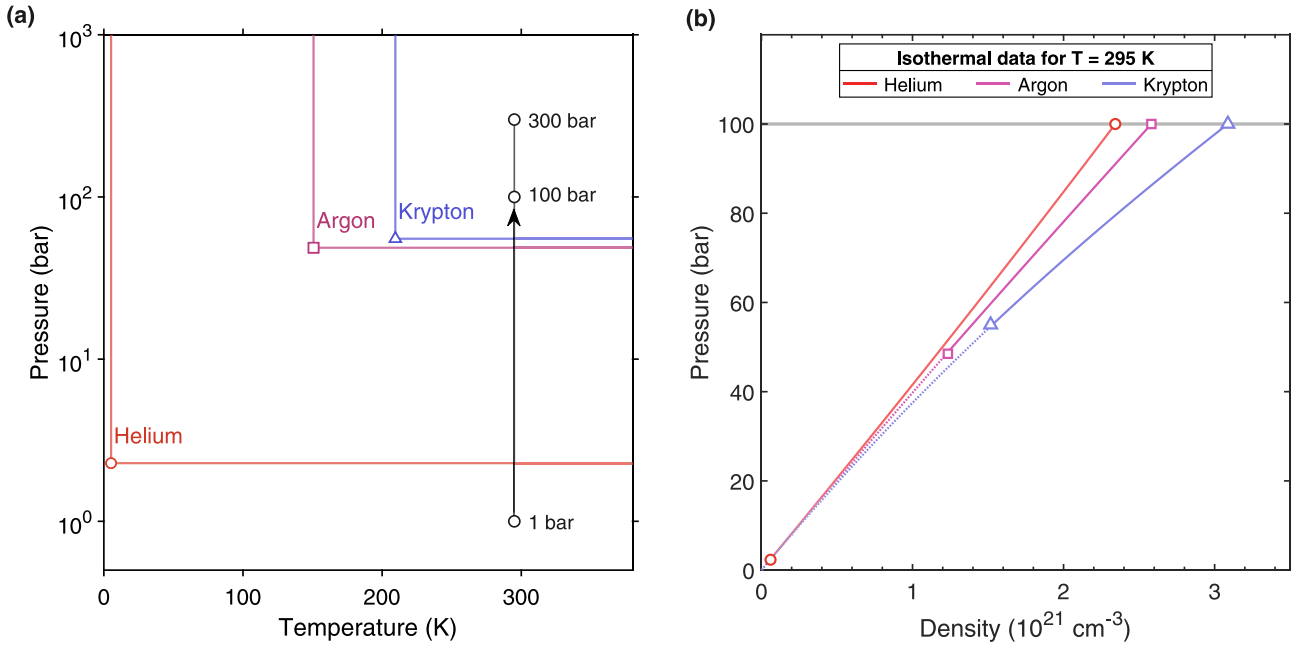

Fig. 1. Thermodynamic properties of the three noble gases. **a** Phase diagrams of helium, argon, and krypton are illustrated. They exhibit distinct critical points at 5.2 K and 2.3 bar for helium, 150.7 K and 48.6 bar for argon, and 209.5 K and 55.3 bar for krypton, respectively. The experimental pressure range is depicted by the black solid line. The compressor and high-pressure chamber have a capacity for up to 300 bar, but most experiments are conducted at 100 bar pressure, where the supercritical fluid condition is well satisfied for all gases. **b** During the pressurization process from 1 bar to 100 bar, as indicated by the arrow in (a), the density inside the chamber varies differently for each species. The critical point of each gas is marked with a circle (2.3 bar), square (48.6 bar), and triangle (55.3 bar), respectively. Dotted lines represent the gas phase (below the critical point), while solid lines represent the supercritical fluid phase (above the critical point). As the pressure increases, particularly in the case of krypton, the density curve deviates from a linear curve, leading variations in density among different species. Helium and krypton have a 30 % different density at 100 bar where most experiments are conducted. The thermophysical properties of fluid systems are obtained from the NIST Chemistry WebBook[17].

At our laser intensity of $I = 2.5\times10^{12}$ W/cm^2, ionization primarily occurs through multiphoton ionization (strong-field ionization) rather than tunneling ionization (Keldysh parameter $\gamma > 1$)[18]. Although we are in the multiphoton ionization regime, a much higher laser intensity is required for it to become the dominant plasma generation mechanism due to its low cross-section. Hence, avalanche ionization (impact ionization) plays a crucial role. In this process, the electrons generated by multiphoton ionization are accelerated within the laser field, and additional electrons are created through collisions with neutral atoms. In the supercritical fluid where the laser-produced plasma forms, the high density of the medium enhances collisional effects. Note that the number of seed electrons is crucial for the subsequent collisional processes to occur effectively. The laser-produced plasmas generated in supercritical fluids of helium and argon differ due to their difference in the ionization potential energy, which influences the multiphoton ionization process. In particular, the expansion volume of the plasma varies depending on the medium. In the 0 ns images shown in Fig. 2, after the plasma expansion has completed, the length of the argon plasma is approximately 56 % longer than that of the helium plasma. This expansion ratio appears to correlate qualitatively with the ionization potential ratio between helium and argon (helium: 24.59 eV, argon: 15.76 eV). However, other processes such as hydrodynamic expansion, thermal conduction, radiative/recombination loss, and absorption differences between species may also contribute to the observed difference. Additionally, in a 100 bar supercritical fluid environment, the laser energy threshold necessary for plasma generation is notably higher in helium compared to argon. This difference again aligns with the ratio of their ionization potentials. For the same reason, the number of pre-ionized electrons produced in helium via multiphoton ionization is smaller than in argon and krypton cases, resulting in a reduced plasma expansion length.

Strongly coupled plasmas and ionization potential depression

We investigate the optical emission spectra emitted by laser-induced plasmas formed in different supercritical fluids to assess the critical factor for attaining strongly coupled plasmas. The emission spectrum in the range of 230-740 nm is measured with a nanosecond time resolution (Fig. 3a–c). As detailed in the experimental setup section, the collection optics with an optical fiber and a lens array capture emissions from a 0.46 mm^2 area, which is aligned with the region of peak emission intensity. To determine the actual shape and absolute intensity of the plasma spectrum, we calibrated the entire measurement system using an intensity calibration

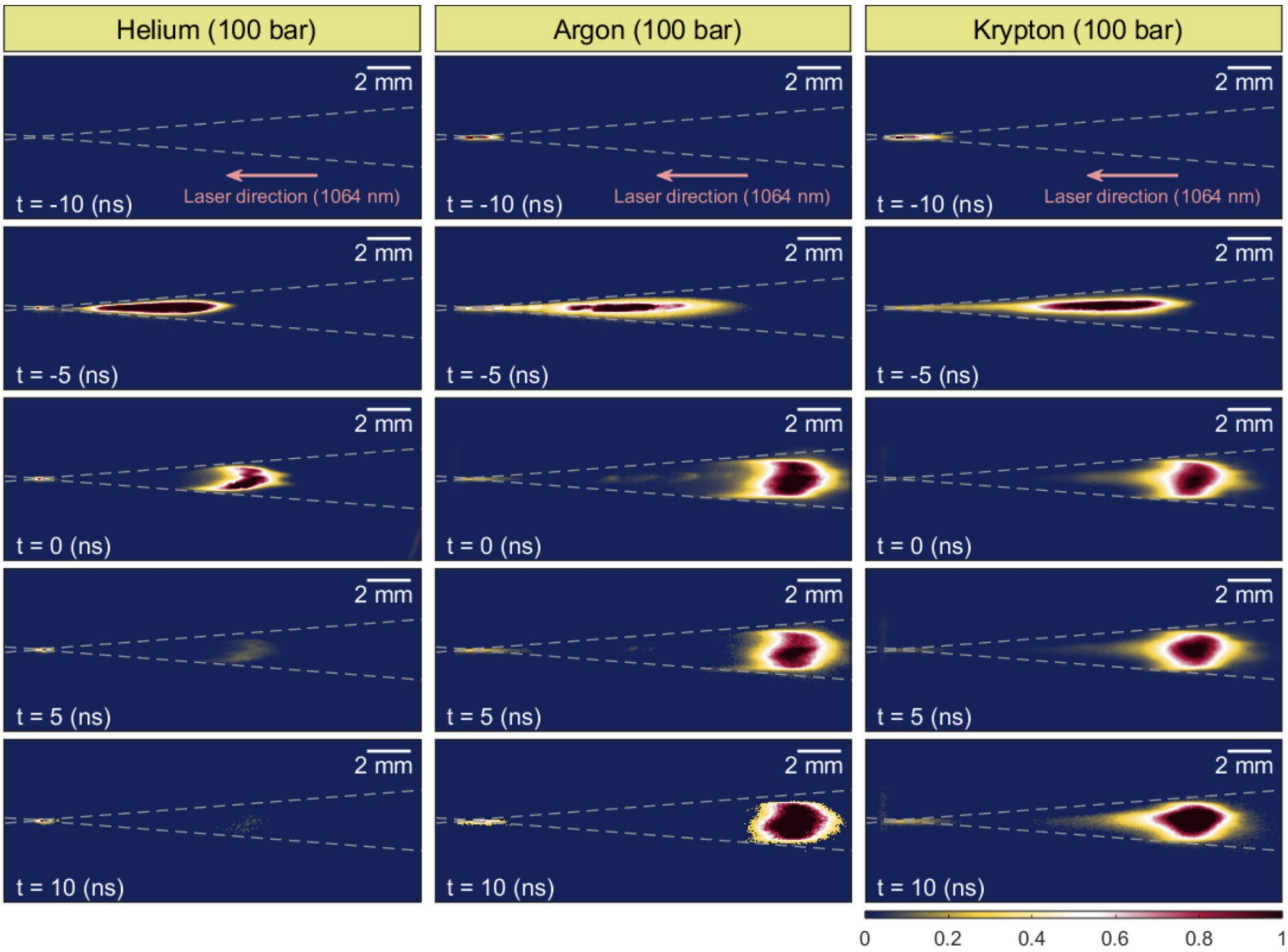

Fig. 2. Time-resolved images of the laser-produced plasma. Each column corresponds to plasma generated in helium, argon, and krypton, respectively. The images are normalized to the maximum intensity at each time frame for all three species. Plasma ignition occurs at -10 ns and expands to the backward direction. The expansion length varies depending on the medium.

source, which includes the optical fiber, monochromator, and ICCD camera. The absolute calibrated spectra are shown in Fig. 3a–c. Interestingly, during the early stage of plasma ($t < 10$ ns), continuum emission dominates, and no line emission is observed, regardless of the medium species. Only at later times ($t > 10$ ns), a few line emissions with strong transition rates emerge above the continuum emission, such as the helium line at 587.5 nm ($3d^3[D]_3 \rightarrow 2p^3[P]^o_2$) and the argon lines at 696.5 nm and 706.7 nm ($4p^2[1/2]_1 \rightarrow 4s^2[3/2]^o_2$ and $4p^2[3/2]_2 \rightarrow 4s^2[3/2]^o_2$). Krypton plasma also exhibits strong line emissions at 760 nm and 811 nm, but these near-infrared wavelengths are beyond the range of the OES measurement. Other atomic lines at 557 nm and 587 nm lines become detectable at 100 ns.

Furthermore, the continuum emissions reveal that the spectra are fitted well with the blackbody radiation formula,

$$B_\lambda(T) = \frac{2\pi hc^2}{\lambda^5\{\exp(hc/\lambda k_B T) - 1\}}, \tag{1}$$

where h, c, λ, k_B, and T are the Planck constant, the speed of light, the wavelength, the Boltzmann constant, and the blackbody temperature, respectively. If the thermal equilibrium is satisfied (that is, the photon travels much longer length than $1/\alpha_\lambda$ to escape dense plasma, where α_λ is the extinction coefficient), the blackbody radiation is described by

$$I = \varepsilon B_\lambda(T), \tag{2}$$

where I is the spectral irradiance, and ε is the emissivity[14,19]. The extinction coefficient of the plasma, analogous to the emissivity ε, indicates how closely the plasma resembles an ideal blackbody in thermal equilibrium. The continuum lines, fitted with a 90 % confidence interval, are shown in Fig. 3a–c, demonstrating that the plasma exhibits near-ideal blackbody radiation. Note that the emissivity and temperature represent the spectrum

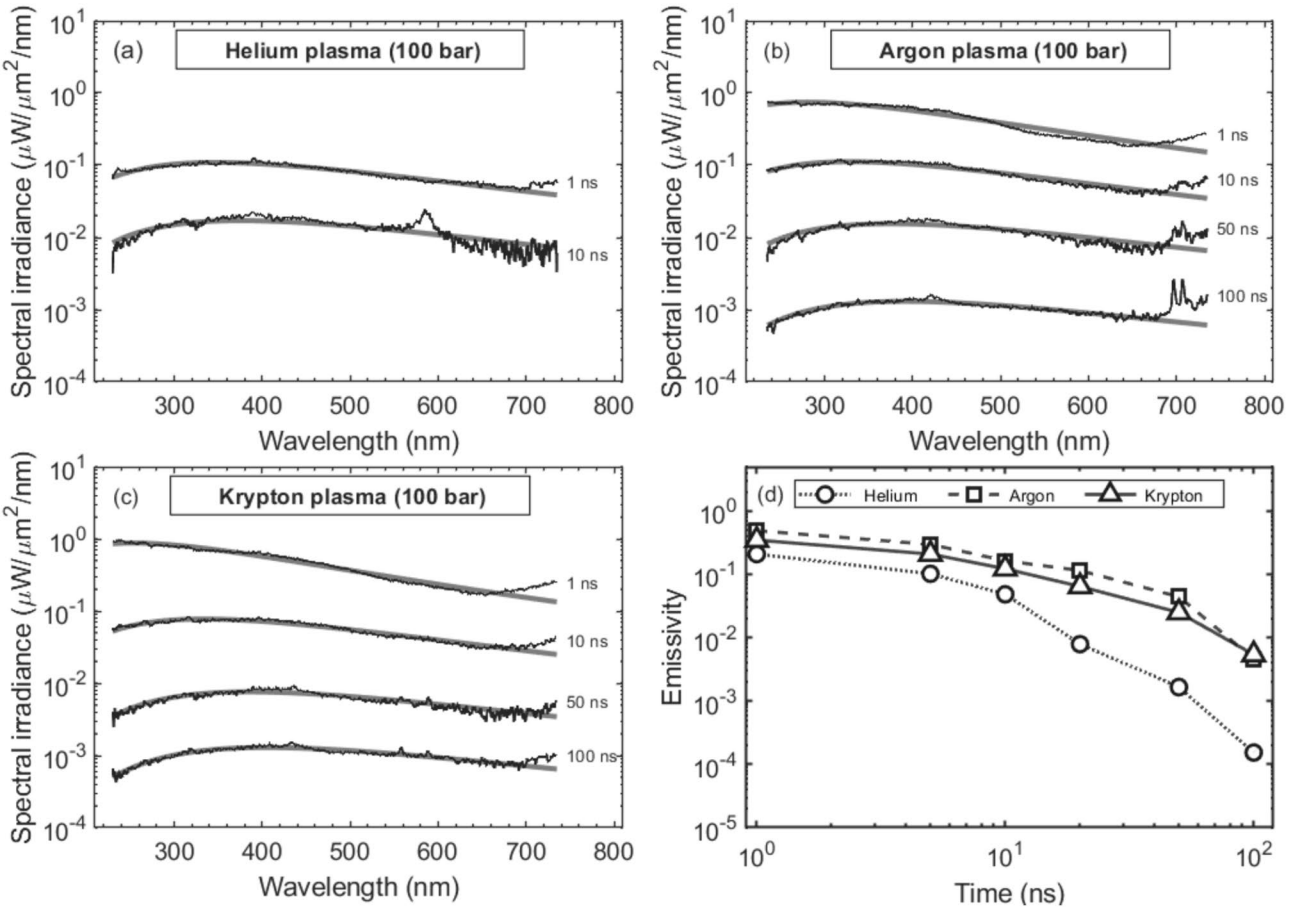

Fig. 3. Optical emission spectroscopy results. Absolutely calibrated emission spectra from the plasmas generated in **a** helium, **b** argon, and **c** krypton supercritical fluids. The fitted blackbody emission curve to the 230–650 nm spectral region is described by a thick gray line. Only the continuum emission is measured unless the line emissions. The spectrum for helium plasma is plotted only up to 10 ns because the decay is much faster compared to other plasmas, such as argon and krypton plasma. **d** Emissivity of the plasmas as a function of time. The emissivities starting around 1 implies that the plasma begins as a gray body, and the emissivity of helium plasma decreases at the fastest rate, indicating the loss channel of the electrons are abundant in helium supercritical fluid case compared to the argon or krypton case.

intensity and the overall slope, respectively. Figure 3d illustrates the relaxation of emissivity over time, suggesting high absorptivity is satisfied only in the initial phase. The opaque plasma rapidly becomes transparent within tens of nanoseconds.

The high absorptivity provides a compelling evidence for very high electron densities. It is well established that within free-bound transitions, three-body recombination becomes the dominant process as the electron density rises[20]. For instance, in the case of a high-density plasma with $n_e = 10^{21}$ cm^{-3} and a relatively low-temperature plasma with $k_B T_e = 1$ eV, the three-body recombination rate and the radiative recombination rate are calculated to be $1 \times 10^{16} s^{-1}$ and 3×10^8 s^{-1}, respectively[21,22]. Thus, in nanosecond timescales, radiation is dominated by three-body recombination processes of electrons and ions. Three-body recombination occurs when an electron is captured by an ion with another electron as the third particle. The recombination time scale τ_{rec} is given by[23]

$$\tau_{rec} = (\bar{v}_e \pi^2 r_0^5 \bar{Z}^4 n_0^2)^{-1}, \tag{3}$$

where $\bar{v}_e$ is the mean thermal electron speed, r_0 is the impact parameter for the three-body recombination collision, $\bar{Z} = n_e/n_0$ is the degree of ionization, and n_0 is the atomic number density of the medium. If we take the impact parameter r_0 derived from the electron-ion collision cross section $\sigma = (\bar{Z} n_0 \bar{v}_e \tau_{ei})^{-1}$, the time scale for three-body recombination is nearly equivalent to the electron-ion collision time scale, which can be calculated by[23]

$$\tau_{ei} = \left[\frac{2}{\sqrt{6\pi}} \omega_p \Gamma^{3/2} \ln \left(\frac{0.7}{\sqrt{3}} \Gamma^{-3/2} + 1 \right) \right]^{-1}. \tag{4}$$

Using the estimated electron density and temperature conditions, the electron-ion collision time is on the order of a few femtoseconds. Considering the mass of the ions, their thermalization may take longer, but this still represents a much faster timescale compared to the experimental time scale. Therefore, we conclude that ionization occurs under an ideal LTE condition in the plasma. The high absorptivity of the plasma is accompanied by rapid thermalization in the dense plasma system[19].

We propose that the abundance of electrons is attributed to an ionization potential depression (IPD) process. When charged particles are sufficiently close to each other and their energy states overlap, the potential levels become perturbed and decreased[22,24]. This phenomenon, known as ionization potential depression, is commonly observed in dense plasmas. Due to its significance, numerous studies have been conducted to directly observe or predict the extent of this effect[25]. However, most of these studies have focused on plasmas from solid targets impacted by intense laser pulse ($I \approx 10^{17}$ W/cm^2). In contrast, to our knowledge, there have been scarce investigations into whether similar ionization potential depression occurs in the context of supercritical fluid environments using a laser of modest intensity ($I \approx 10^{12}$ W/cm^2). Strong electron-electron interactions cause the collapse of energy states, thereby preventing the occurrence of line emissions resulting from electron transitions between energy states. The delayed appearance of line emissions suggests that ionization potential depression is manifesting. The dense system undergoes thermalization within a transient period, absorbing and emitting photons similar to a blackbody.

Regardless of the composition, the emissivity reaches approximately 0.5, as the laser energy is sufficient to achieve the blackbody condition during the plasma generation phase. On the other hand, the relaxation speed depends on the gas species. As shown in the plasma images in Fig. 2, the rapid decay of emissivity in helium plasma corresponds to the swift extinction of its emission. Different relaxation speeds in other gas species indicate that the relaxation mechanism is influenced by several factors, particularly the amount of ionization potential depression and the initially coupled laser energy. Moreover, even during the generation stage (1 ns), plasma temperatures show noticeable differences (See Table. 1). To estimate the electron density of the plasma generated in each supercritical fluid, we employ the ionization potential depression model in dense plasmas and the modified Saha's equation, using temperatures derived from the blackbody analysis. The amount of potential lowering is given by[22–24]

$$\Delta\chi = \frac{(\bar{Z}+1)e^3}{4\pi\varepsilon_0}\sqrt{\frac{\bar{Z}(\bar{Z}+1)n_0}{\varepsilon_0 k_B T_e}}. \tag{5}$$

Saha's equation describes the relationship of the energy state population in LTE condition. By applying eq. (5), Saha's equation is corrected as

$$\frac{\bar{Z}^2}{1-\bar{Z}} = \frac{2}{n_0}\frac{u_1}{u_0}\left(\frac{m_e k_B T_e}{2\pi h^2}\right)^{3/2}\exp\left(-\frac{\chi_0-\Delta\chi}{k_B T_e}\right), \tag{6}$$

where $\Delta\chi$ is the amount of the ionization potential depression and χ_0 is the ionization potential of the neutral atom. Since we have two equations, we can express the two parameters as the function of temperature. The degree of ionization generated in each supercritical fluid is shown in Fig. 4. The markers represent the plasma temperature estimated from the blackbody analysis. By solving Eqs. 5 and 6 simultaneously, we obtain the degrees of ionization: $\bar{Z}_{He} \approx 0.7$, $\bar{Z}_{Ar} \approx 0.5$, $\bar{Z}_{Kr} \approx 0.4$, and the ionization potential depression: $\Delta\chi_{He} \approx$ 24 eV, $\Delta\chi_{Ar} \approx 13$ eV, $\Delta\chi_{Kr} \approx 12$ eV (Table 1). A large reduction in potential means that there is little energy cost for ionizing the medium. According to the calculated degrees of ionization and the medium density, we obtain electron densities as $n_e \approx 1.94\times 10^{21}$ cm^{-3}, 1.22×10^{21} cm^{-3}, 1.05×10^{21} cm^{-3} for helium, argon, and krypton, respectively. The dominant source of error in estimating electron density from IPD calculations arises from the blackbody fitting used for temperature measurement. This temperature uncertainty propagates to the IPD and electron density estimates. However, as shown in Table 1, the resulting error in electron density is negligible. The plasma density decreases in the order of helium, argon, and krypton, while the plasma temperature increases in the same order. Although helium has the lowest neutral density at 100 bar (Fig. 1b), it is noteworthy that the electron density of the helium plasma is twice that of the krypton plasma. These values result in Coulomb coupling parameters of $\Gamma_{He} \approx 4.0$, $\Gamma_{Ar} \approx 2.8$, and $\Gamma_{Kr} \approx 2.5$. The calculated Coulomb coupling parameters exceeding unity (1), in turn, support the validity of the electron density estimation based on the ionization potential depression model.

Species	Temperature (K)	Ionization potential (eV)	IPD (eV)	Degree of ionization	Electron density (cm^{-3})
Helium	8321 ± 78	24.59	23.85 ± 0.01	0.83	(1.94 ± 0.08) ×10^{21}
Argon	10342 ± 184	15.76	12.85 ± 0.07	0.47	(1.22 ± 0.01) ×10^{21}
Krypton	10937 ± 180	14.00	11.61 ± 0.08	0.34	(1.05 ± 0.01) ×10^{21}

Table 1. Plasma parameters with three noble gases. Plasma temperature is from a blackbody analysis. The amount of ionization potential depression and the degree of ionization are calculated by the potential lowering model in the dense plasma and the modified Saha's equation. In the case of helium plasma, ionization can occur with energies even lower than 1 eV. All plasmas have a high electron density with an order of 10^{21}cm^{-3}.

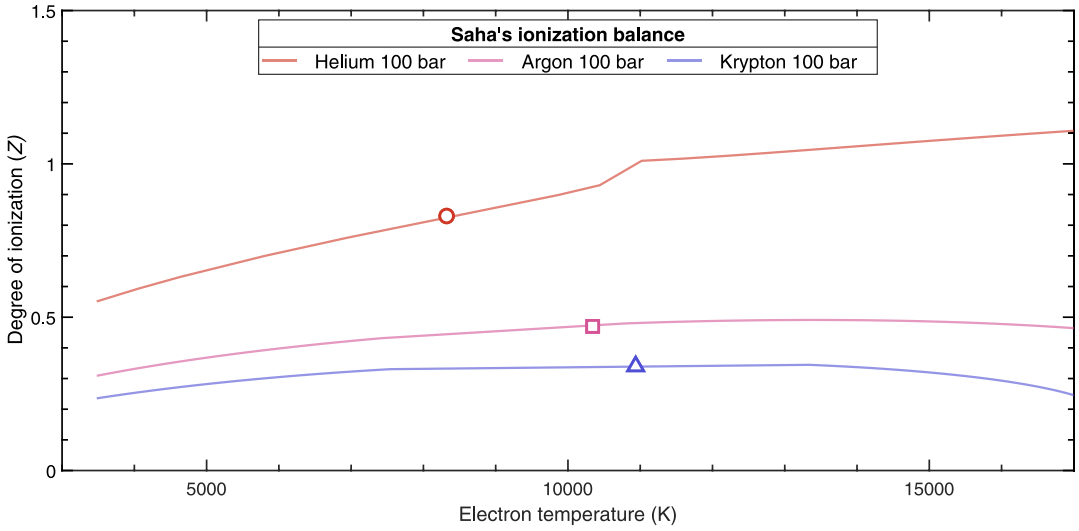

Fig. 4. Result of the ionization potential depression model. The degree of ionization is a function of temperature. The plasmas generated in helium, argon, and krypton supercritical fluids have distinct ionization levels. The measured plasma temperatures are indicated by the symbol markers. Combining with the neutral densities, the estimated electron densities are shown in Table 1. The error in the degree of ionization resulting from temperature fitting is smaller than the marker size and therefore not indicated in the figure.

The electron density is highest in the helium supercritical fluid, gradually decreasing with argon and krypton. Given that helium exhibits the highest ionization potential depression (≈24 eV), it is plausible to assume that the extent of ionization potential depression, influenced by perturbation from surrounding charged particles, plays a crucial role in achieving high electron density. If a sufficient electron density is achieved during the generation phase, the IPD process enables the production of abundant electrons from atoms, further increasing the electron density. Despite helium having the lowest laser coupling energy and neutral particle density, its highest electron density highlights the significance of IPD.

Discussion

Electron density measurement using UV interferometry

In this study, various methods confirmed that the laser produced plasmas in supercritical fluid media attain sufficiently high electron density satisfying the strongly coupled condition. First, the emissivity close to unity indicates that the electron density is large enough to create a highly collisional environment, leading to substantial photon absorption. Second, the absence of line emissions in the early stages of plasma formation suggests that the electron density is so high that the IPD effect is dominant. Lastly, more direct evidence is obtained through theoretical estimation using the amount of IPD values, which confirms that the plasma density is of the order of 10^{21} cm^{-3}, thereby satisfying the strongly coupled condition. However, these approaches rely on indirect observations and estimations based on the IPD model for electron density. To directly measure the high electron density and validate the IPD model, we performed interferometric measurements using a pulsed UV laser. As depicted in Fig. 5a, the interferometer is a Mach–Zehnder type setup. A 266 nm pulsed laser (the 4th harmonic Nd:YAG laser) is used in a pump-probe configuration. Since the critical density is inversely proportional to the square of the wavelength, using a shorter wavelength laser allows for a higher critical density. For a 266 nm laser, the critical density corresponds to 10^{22} cm^{-3}. The probe laser is split into two paths by the first beam splitter: one arm passes through the high-pressure chamber while the other bypasses it. The two beams are recombined at the second beam splitter, forming an interference pattern. The laser-produced plasma by the pump laser alters the refractive index of the medium, which can be given by

$$N = \sqrt{1 - \frac{n_e}{n_c}}, \tag{7}$$

where $n_c = m_e \varepsilon_0 \omega^2 / e^2$ is the critical density[26]. This change in the refractive index affects the phase of the probe laser passing through it, leading to a shift in the fringe pattern. Therefore, the fringe shift provides information about the electron density of the plasma. However, an unexpected result is observed during the early stages of plasma formation, when the estimated electron density is high enough to be a strongly coupled plasma. Rather than shifting, the fringe pattern completely disappeares in helium, argon, and krypton plasmas (Fig. 5b–d). This phenomenon is likely due to the high electron density in all cases at the initial stage of plasma generation. As shown in Eq. (7), when the electron density approaches the critical density, the change in the refractive index becomes so significant that the refraction of the UV probe beam is pronounced, preventing the light from reaching the CCD camera. Moreover, a strong absorption in the UV range is expected. Although quantitative electron density measurements are not obtained using the fringe shift method, this observation confirms that

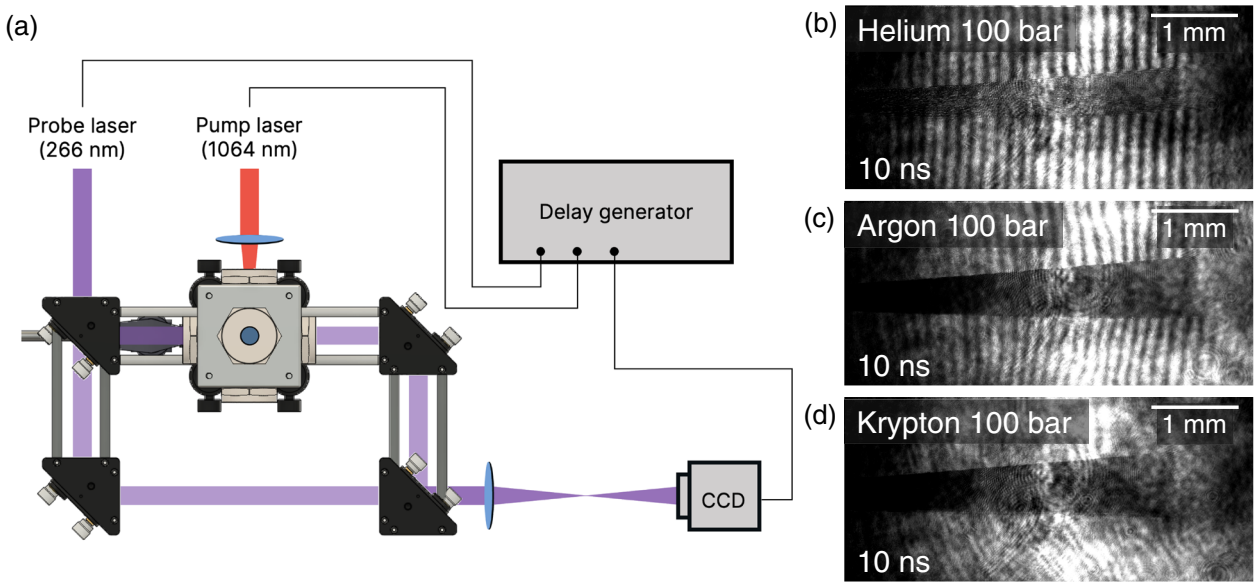

Fig. 5. UV interferometer for electron density estimation. **a** Schematic of the Mach-Zehnder interferometer, created using the 3D design software. The pump laser (red) is focused at the center of a high-pressure chamber filled to 100 bar, while the probe laser (purple) is split into two beams. These beams travel along separate paths and recombine, producing a fringe pattern. The delay generator synchronizes the timing of the pump laser, probe laser, and CCD camera, ensuring precise measurement. Fringe patterns observed in supercritical fluids of **b** helium, **c** argon, and **d** krypton. The fringe signal generated by the UV laser is obstructed within the plasma region.

the laser plasmas generated in various supercritical fluids reach sufficiently high electron densities to qualify as strongly coupled plasmas. A new interferometry or scattering scheme using a much shorter wavelength than 266 nm will be necessary to overcome the limitations of the present fringe counting method and verify the electron densities estimated from the IPD model.

Conclusion

In this work, we have introduced an effective method for generating strongly coupled plasmas with high density, achieving $\Gamma \sim 4$, in supercritical fluids of various species (helium, argon, and krypton). Our study emphasizes the critical role of ionization potential depression in attaining the electron densities necessary for strongly coupled plasmas. A noteworthy finding is the remarkable effectiveness of helium, a prevalent element in stars and throughout the universe, in achieving high electron densities. Our results indicate that the ionization potential depression operates most efficiently in helium, suggesting that this mechanism could provide useful insight into the behavior of plasmas in astrophysical environments, including the interiors of stars, where strongly coupled states may occur. Our novel experimental approach, utilizing high-pressure supercritical fluids, represents a significant advancement in this field, promising to deepen understanding of strongly coupled plasmas.

Methods

Acquisition setting

The ICCD camera (Teledyne Princeton Instruments PI-MAX4) is used for optical diagnostics, including imaging and spectroscopy. With a minimum gate width of 3 ns and an intensifier, the camera enables nanosecond time-resolved measurements. To synchronize the timing between plasma generation and image acquisition, we use the output signal from the Q-switch of the Nd:YAG pulsed laser (Quantel Brilliant b), which precedes the laser pulse emission. The optical magnification of the lens array is approximately 0.7 for the imaging results shown in Fig. 2 with a fixed intensifier gain of 1. The camera captures images by delaying the gate from –15 ns to 50 ns in 1 ns increments. Among these, the frames at –10, –5, 0, 5, and 10 ns are displayed in Fig. 2. For the OES measurements shown in Fig. 3, we use an optical fiber (Thorlabs M114L01) with a numerical aperture of 0.22 and a core diameter of 600 μm. A focusing lens defines the collection area of the focal spot approximately 0.43 mm^2. Table 2 summarizes the acquisition settings used for each time delay in the OES measurements. At longer delays, the gate width and signal averaging are increased to compensate for the weaker emission and reduced temporal variation. Each OES spectrum is averaged over multiple discharges to improve the signal-to-noise ratio, while each image represents a single laser shot.

Absolute calibration process

To determine the absolute intensity of the measured spectra, an absolute calibration light source (Ocean Optics DH-3 Plus) is used. This source contains a deuterium lamp and a halogen lamp, which provide known spectral irradiance in the UV (210–400 nm) and VIS-NIR (350–1100 nm) ranges, respectively. The spectral irradiance

Time (ns)	Gate width (ns)	Accumulation	Exposures per frame (avg.)	Gain
1, 5, 10, 20	3	1	10	10
50	5	1	20	20
100	10	3	30	30

Table 2. Acquisition settings for spectroscopy.

emitted by the lamp is provided in units of $\mu W/cm^2/nm$. By comparing the spectrum of the calibration lamp with the known spectral irradiance, the spectral response function of the optical system (optical fiber, monochromator, and ICCD camera) can be obtained. The spectral response of the measurement system is absolutely calibrated with an uncertainty of ±15 % using this standard light source. This response function accounts for the spectral response of each component in the detection system. It is applied to the plasma emission spectra to obtain intensity-calibrated spectra. This calibration enables a quantitative comparison of spectral intensities and allows for accurate analysis of the plasma emission characteristics.

Data availability

All relevant data supporting this study are available from the authors (J.L. and G.Y.) upon reasonable request.

Received: 13 April 2025; Accepted: 29 October 2025
Published online: 27 November 2025

References

1. Ichimaru, S. Strongly coupled plasmas: high-density classical plasmas and degenerate electron liquids. *Rev. Mod. Phys.* **54**, 1017–1059. https://doi.org/10.1103/RevModPhys.54.1017 (1982).
2. Kowalski, P. M., Mazevet, S., Saumon, D. & Challacombe, M. Equation of state and optical properties of warm dense helium. *Phys. Rev. B* **76**, 075112. https://doi.org/10.1103/PhysRevB.76.075112 (2007).
3. Saumon, D., Blouin, S. & Tremblay, P.-E. Current challenges in the physics of white dwarf stars. *Phys. Rep.* **988**, 1–63 (2022).
4. Ichimaru, S. Theory of strongly correlated charged-particle systems: Plasma turbulence and high-density electron liquids. *Phys. Rev. A* **15**, 744–754. https://doi.org/10.1103/PhysRevA.15.744 (1977).
5. Horn, H. M. V. Dense astrophysical plasmas. *Science* **252**, 384–389. https://doi.org/10.1126/science.252.5004.384 (1991).
6. Murillo, M. S. Strongly coupled plasma physics and high energy-density matter. *Phys. Plasmas* **11**, 2964–2971. https://doi.org/10.1063/1.1652853 (2004) https://pubs.aip.org/aip/pop/article-pdf/11/5/2964/12335238/2964_1_online.pdf.
7. Daligault, J. On the quantum Landau collision operator and electron collisions in dense plasmas. *Phys. Plasmas* **23**, 032706. https://doi.org/10.1063/1.4944392 (2016).
8. Ji, J.-Y. Closure theory for high-collisionality multi-ion plasmas. *Plasma Phys. Control. Fusion* **65**, 075014. https://doi.org/10.1088/1361-6587/acd8ee (2023).
9. Dimonte, G. & Daligault, J. Molecular-dynamics simulations of electron-ion temperature relaxation in a classical coulomb plasma. *Phys. Rev. Lett.* **101**, 135001. https://doi.org/10.1103/PhysRevLett.101.135001 (2008).
10. Baalrud, S. D. & Daligault, J. Effective potential theory for transport coefficients across coupling regimes. *Phys. Rev. Lett.* **110**, 235001. https://doi.org/10.1103/PhysRevLett.110.235001 (2013).
11. Grabowski, P. E., Surh, M. P., Richards, D. F., Graziani, F. R. & Murillo, M. S. Molecular dynamics simulations of classical stopping power. *Phys. Rev. Lett.* **111**, 215002. https://doi.org/10.1103/PhysRevLett.111.215002 (2013).
12. Lyon, M., Bergeson, S. D., Hart, G. & Murillo, M. S. Strongly-coupled plasmas formed from laser-heated solids. *Sci. Rep.* **5**(1), 15693. https://doi.org/10.1103/PhysRevLett.11.401 (2015).
13. Meyerand, R. G. Jr. & Haught, A. F. Gas breakdown at optical frequencies. *Phys. Rev. Lett.* **11**(9), 401 (1963).
14. Lee, S., Lee, J., Yoon, Y. D., Kim, D. E. & Yun, G. Characterization of strongly coupled plasmas produced in argon supercritical fluids. *Plasma Phys. Control. Fusion* **64**, 095010. https://doi.org/10.1088/1361-6587/ac7ee8 (2022).
15. Lee, S. et al. Quasi-equilibrium phase coexistence in single component supercritical fluids. *Nat. Commun.* **12**(1), 4630. https://doi.org/10.1038/s41467-021-24895-y (2021).
16. Lee, J. et al. Experimental evidence of non-equilibrium phase separation in supercritical fluids. *Commun. Phys.* **8**, 341. https://doi.org/10.1038/s42005-025-02263-2 (2025).
17. Linstrom, P. J. & Mallard, W. G. *NIST Chemistry WebBook, NIST Standard Reference Database Number 69* (National Institute of Standards and Technology, Gaithersburg MD, 20899, 2024).
18. Augst, S., Strickland, D., Meyerhofer, D. D., Chin, S. L. & Eberly, J. H. Tunneling ionization of noble gases in a high-intensity laser field. *Phys. Rev. Lett.* **63**, 2212–2215. https://doi.org/10.1103/PhysRevLett.63.2212 (1989).
19. Yasui, K. Mechanism of single-bubble sonoluminescence. *Phys. Rev. E* **60**, 1754–1758. https://doi.org/10.1103/PhysRevE.60.1754 (1999).
20. Giacomo, A. D., Gaudiuso, R., Dell'Aglio, M. & Santagata, A. The role of continuum radiation in laser induced plasma spectroscopy. *Spectrochim. Acta Part B: At. Spectrosc.* **65**, 385–394 (2010).
21. Richardson, A. S. *NRL Plasma Formulary* (2019).
22. Zel'dovich, Y. P. & Raizer, Y. B. *Physics of Shock Waves and High-Temperature Hydrodynamic Phenomena* (Dover, New York, 1966).
23. Bataller, A., Plateau, G. R., Kappus, B. & Putterman, S. Blackbody emission from laser breakdown in high-pressure gases. *Phys. Rev. Lett.* **113**, 075001. https://doi.org/10.1103/PhysRevLett.113.075001 (2014).
24. Griem, H. R. High-density corrections in plasma spectroscopy. *Phys. Rev.* **128**, 997–1003. https://doi.org/10.1103/PhysRev.128.997 (1962).
25. Ciricosta, O. et al. Direct measurements of the ionization potential depression in a dense plasma. *Phys Rev Lett.* **109**, 065002. https://doi.org/10.1103/PhysRevLett.109.065002 (2012).
26. Hutchinson, I. H. *Principles of Plasma Diagnostics* 2nd edn. (Cambridge University Press, 2002).

Acknowledgements

This work was supported by the National Research Foundation of Korea (NRF) grant funded by the Ministry of Science and ICT (RS-2024-00349684 and RS-2022-NR070637). This work was also supported by the Glocal University 30 project funded by the Ministry of Education.

Author contributions

G.Y. proposed the original idea and conceived the project. J.L. designed the laser plasma experiments under high-pressure conditions. J.L., H.L., S.K., and H.S. designed and conducted time-resolved UV interferometer experiments to measure the electron density of strongly coupled plasmas. J.L. carried out the data processing and analysis. J.L. wrote the draft of the manuscript. G.Y. supervised the project. All authors contributed significantly to the discussion of the results. All authors reviewed the manuscript.

Declarations

Competing interests

The authors declare no competing interests.

Additional information

Correspondence and requests for materials should be addressed to G.Y.

Reprints and permissions information is available at www.nature.com/reprints.

Publisher's note Springer Nature remains neutral with regard to jurisdictional claims in published maps and institutional affiliations.